Soft Matter

RSC Publishing

PAPER

Cite this: *Soft Matter*, 2013, **9**, 8005

Chirality inversions in self-assembly of fibrillar superstructures: a computational study†

Magdalena Gruziel,[ab] Wojciech Dzwolak[c] and Piotr Szymczak*[a]

Received 28th December 2012
Accepted 11th June 2013

DOI: 10.1039/c3sm27961h

www.rsc.org/softmatter

The formation of aggregates of helical fibrils is analyzed numerically. The aggregate morphology, chirality and stability are studied as a function of temperature and helical pitch of individual fibrils. The simulations show the existence of a critical pitch above which the handedness of the aggregates is opposite to that of the constituting fibrils. We also observe and analyze the process of spontaneous chirality inversion of individual fibrils within the aggregates. This inversion is accompanied by a helical wave propagating along the fibril axis, with a kink separating left-handed and right-handed regions moving along the fibril. The frequency of this process is strongly dependent on the initial pitch of the fibrils with a local maximum near the critical pitch.

1 Introduction

Chiral macromolecules can undergo hierarchical self-organization, a process that gives rise to chiral superstructures stabilized by intermolecular interactions.[1–3] Understanding the basic parameters that govern this self-assembly process is important both from the fundamental point of view and for potential applications in "bottom-up" nanoengineering. The key question in this context is how does the chirality of the superstructure depend on the chiralities of the constituent units, the presence of chiral templates in the system and the dynamics of the aggregation process itself.[4–6]

A fascinating aspect of biological chiral superstructures emerged when amyloid fibrils – elongated aggregates of misfolded protein molecules that are typically associated with degenerative disorders such as Alzheimer's, or Parkinson's disease[7] – were shown to have either right- or left-handed helical morphology.[8] Interestingly, these distinct structures turned out to be accessible to amyloid-forming chirally-biased polypeptide chains composed entirely of L-amino acid residues. Thus the notion expressed in earlier works that the chiral bias of polypeptide chains would predispose, in a deterministic fashion, self-assembling protein molecules to form higher-order structures of one preferred handedness turned out to be incorrect.[9] Presently, for a given polypeptide chain, the permitted helical traits of a resulting amyloid structure are thought to be manifold and tunable by environmental factors.[10–12] Recent studies show that shifting the delicate balance of intramolecular interactions stabilizing a particular chiral mode of self-assembled amyloid fibril may lead to its dramatic reorganization and simultaneous reversal of optical activity probed by vibrational circular dichroism – a physical property strongly linked to chirality of superstructures.[11,12] In particular, this holds true for vortex-induced chiral superstructures of insulin amyloid fibrils which may exhibit either strongly negative or strongly positive electronic circular dichroism.[13–16] While the relationship between the assembly pathway of individual fibrils and the chirality of higher order structures remains poorly understood, this knowledge is urgently needed not only out of purely fundamental interest, but also in the context of possible applications of chiral amyloid superstructures as novel helical metamaterials.[17,18]

In this article, we study these questions using a simple model of fibrillar structures inspired by the molecular architecture of insulin fibrils. Recent experiments on insulin aggregation have revealed a structural transition in insulin fibrils,[13–15] with two types of superstructures with opposite chiralities formed. The transition seems to be controlled by both the temperature and the intensity of agitation (turbulent mixing) in the system, however the details of this process are still uncertain.

Despite the rapid increase in computer power, the computational demands are still a barrier, preventing atomistically detailed simulations of the self-assembly process due to the large system sizes and long timescales involved. This motivated the use of a coarse-grained model of the aggregating biopolymers in the present study. In the model, the filament backbone is represented by a chain of beads, whereas a second type of beads is used to represent the attractive interaction sites, arranged in two strips on the opposite sides of the backbone, each helically wound along the length of the fibril. This

---

[a] *Institute of Theoretical Physics, Faculty of Physics, University of Warsaw, Hoza 69, 00-618, Warsaw, Poland. E-mail: piotr.szymczak@fuw.edu.pl*

[b] *Interdisciplinary Centre for Mathematical and Computational Modeling, University of Warsaw, Pawińskiego 5a, 02-816, Warsaw, Poland*

[c] *Department of Chemistry, University of Warsaw, Pasteura 1, 02-093 Warsaw, Poland*

† Electronic supplementary information (ESI) available. See DOI: 10.1039/c3sm27961h

structure is related to the model of insulin protofilaments proposed by Ivanova *et al.*[19] (*cf.* Fig. 5 therein), where the spine of the protofilament is composed of a steric zipper of β-strands, and the floppy C-termini of insulin chain B on the opposite sides of the filament wind around the filament axis. Because these termini are both hydrophobic and capable of associating into interchain molecular velcro they tend to be attractive.[20]

The aggregation of the filaments has been studied using Langevin dynamics. Particular attention was paid to the evolution of the chirality during the aggregation process. Despite the simplicity of the adopted model, the dynamics turns out to be nontrivial, with hierarchical, scale-dependent chirality of the resulting structures. A major role in the emergence of chiral ordering within the aggregates is played by the chirality inversion events, either spontaneous or triggered by the interaction with other fibrils in the cluster. These processes provide a way for the individual fibrils in the cluster to adjust their chiralities so that they match up.

The paper is organized as follows. Section 2 details the numerical model of aggregating filaments used in the present study. The aggregation process and the resulting morphologies of the clusters are studied in Section 3. Next, in Section 4 we analyze the dynamics of the chirality inversion process. Finally, the conclusions are drawn in Section 5.

2 The model

The coarse-grained model of protein fibrils adopted in this work is presented schematically in Fig. 1a. The grey beads represent the backbone of the fibril (B) whereas the white beads represent the attractive interaction sites (S), forming two strips helically wound around the backbone. For the sake of brevity, we shall refer to these strips as "side-strands".

In terms of bonding interactions, the force field includes harmonic potentials for both bonds (between consecutive B beads and between B bead and the adjacent S bead) and bond angles (between three consecutive B beads and between two consecutive B beads and one of the adjacent S beads). The detailed description of the forcefield can be found in the ESI,† where the most significant features are presented.

The key element of the model is the introduction of a symmetric double well dihedral potential U_θ associated with the dihedral angle spanned by four consecutive beads S1 – B_i – B_{i+1} – S2 and denoted as θ in Fig. 1a, where S1 and S2 mark the beads of the two opposite helical side strands. The potential has two minima at $\theta = \pm\theta_0$ inducing local twist of the side strands. This potential alone, however, is not enough to impose a global chirality on the molecule, since the values of the consecutive dihedrals are uncorrelated and thus the global twist will average out to zero. To prevent that, we introduce another dihedral potential, U_λ, this time associated with the circumferential angle between two neighboring S beads belonging to the same strand, *i.e.* spanned by S – B_i – B_{i+2} – S (*cf.* Fig. 1a). This potential has the minima at $\pm\lambda_0 = \pm 2(\pi - \theta_0)$ and a barrier at $\lambda = 0$ with barrier height $\Delta U_\lambda = U(0) - U(\pm\lambda_0) = k_\lambda \lambda_0^2/2$. Together, the two dihedral potentials can lead to a chiral symmetry breaking and spontaneous appearance of a nonzero torsion of the filament side strands. The torsion is defined as the circumferential angle between the two neighboring side strand beads divided by the corresponding backbone distance, $\tau = \lambda_0/2l_{BB}$, where l_{BB} is the distance between the backbone beads. In practice, it will be advantageous to characterize the twist not in terms of λ, but rather the helix angle α, which is the angle between the helix and the cylinder axis (see Fig. 1b), with $\alpha_0 = \arctan(\lambda_0)$ (for the derivation see the ESI†).

Another important element of the model is Lennard-Jones interaction between the beads belonging to different molecules:

$$U_{LJ} = 4\varepsilon\left[\left(\frac{\sigma}{r}\right)^{12} - \left(\frac{\sigma}{r}\right)^{6}\right] \tag{1}$$

these forces are responsible for the aggregation of the filaments and the formation of superstructures. We use the uniform energy scale for backbone and side strand beads $\varepsilon_B = \varepsilon_S = \varepsilon$ but different length scales: $\sigma_B = 4\sigma_S$. The Lorentz–Berthelot combining rules are used to calculate the cross-species interaction parameters. All results are given in reduced units, where σ_S was used as the length unit and ε as the energy unit. In these units, the equilibrium distance between the backbone beads $l_{BB} = 1$, whereas that between B bead and the adjacent S bead is $l_{BS} = 2$. All the filaments are composed of a fixed number of backbone and side strand beads, $n_B = 2n_{S1} = 2n_{S2} = 60$.

The equilibrium configuration of the backbone is linear, however for the set of parameters considered here the persistence length is of the order of the chain length so that the fibrils are semi-flexible and – as they aggregate – their backbones can themselves become helically distorted.

The trajectories of the filaments are calculated using Langevin dynamics. A natural time scale in the simulations is set by the time it takes for a single bead to diffuse over the distance σ_B, *i.e.* $t_D = \dfrac{\gamma\sigma_B^2}{6k_BT}$, where γ is a single bead friction coefficient. This time scale is used as a time unit in the data reported. The simulations were performed with the use of the LAMMPS[21] molecular dynamics package. In each run, we tracked the

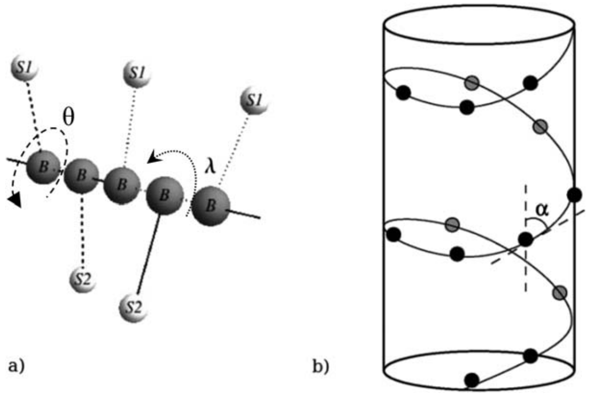

Fig. 1 (a) Sketch of the model, with backbone beads in grey and side strand beads in white. Bonds defining the dihedral angles θ and λ are dashed and dotted, respectively; (b) definition of the helix angle α (for the clarity of the presentation, only one helical side strand is depicted).

connectivities between the filaments (two filaments were assumed connected if the distance between their closest beads was smaller than $3\sigma_S$), sizes of the resulting clusters, and their chiralities (see below). The simulations were run for several values of the reduced temperature, $T^* = k_B T/\varepsilon$. Also, several values of the helix angle α_0 were studied to analyze the impact of the initial fibril twist on the resulting cluster morphology.

A number of different functionals have been proposed as a measure of degree of chirality.[22–27] An appropriate measure of chirality should change the sign on mirror reflection of the molecule, but remain invariant under rotation or translation. Moreover, at least for the helix-like molecules considered here, the magnitude of chirality should be larger the more twisted the helix is. In this paper, we measure the chirality of the chain using the following quantity:

$$\chi = \frac{1}{n}\sum{}' \operatorname{arctan2}\left(|\boldsymbol{v}_i|\boldsymbol{v}_{i-1}\cdot(\boldsymbol{v}_i\times\boldsymbol{v}_{i+1}), (\boldsymbol{v}_{i-1}\times\boldsymbol{v}_i)\cdot(\boldsymbol{v}_i\times\boldsymbol{v}_{i+1})\right), \quad (2)$$

where the sum, $\sum'$, is over all quadruplets of beads $i-1, i, i+1, i+2$ along the chain, n is the total number of such quadruplets, $\boldsymbol{v}_i = \boldsymbol{r}_{i+1} - \boldsymbol{r}_i$ is a vector connecting two consecutive beads, and arctan2(x,y) is the four-quadrant arctangent function (defined as $\arctan(y/x)$ for $x > 0$, $\arctan(y/x) + \pi$ for $y \geq 0$, $x < 0$, and $\arctan(y/x) - \pi$ for $y < 0$, $x < 0$). The above-defined chirality measure has a particularly simple interpretation: it is an average (signed) dihedral angle in the filament associated with each three consecutive vectors along the chain. Moreover, as shown in the Appendix, in the continuous limit χ is proportional to the local torsion of the curve, thus it indeed measures how sharply the curve twists.

It is important to note that the use of scalar functions as chirality measures for objects of arbitrary shape is not without its problems, the most significant of which is that of ‘chiral zeros’ – situations in which a chirality measure turns zero despite the fact that the object is chiral.[28–30] Here, however, we limit ourselves to slightly distorted helical structures, for which chirality can be defined in a self-consistent manner.

The formula (2) can be used to calculate chirality both of the backbone and the side strands. The side strand chirality (which we will also call the first order chirality, $\chi^{(1)}$) is determined to a large extent by the imposed dihedral potential of the filament. On the other hand, the equilibrium configuration of a backbone of a single filament is linear, thus any chirality that it attains is due to the interactions with other filaments and reflects the arrangements of the filaments within the superstructure. This backbone chirality will be called a second order chirality and denoted $\chi^{(2)}$. Due to the stiffness of the backbone the pitch of the helix formed by the backbone beads is usually of the order of the fibril length. This means that the dihedral terms involved in eqn (2) are of a small magnitude and hence noise-dominated. A more meaningful information about the backbone chirality can be obtained by coarse-graining the description and using as $\boldsymbol{v}_i$ in eqn. (2) the vectors joining every eighth backbone bead.

In general, the second order chirality may have not only a different value, but also a different sign from the first order one. There are several examples of natural structures with such non-trivial, scale dependent chirality features: a number of coiled-coil structures (*e.g.* α-keratin, N-terminal HIV-1 gp41 trimer, others[31]) or collagen-like helices are composed of right-handed α-helices winding along each other in a left-handed manner. Notably, however, there are also many coiled-coil structures in which the first- and second-order chiralities agree in sign.[31] Hierarchical chiral structures are also common in cholesteric liquid crystals,[2,32–35] self-assembled structures at the nanoscale[1,5,36] or in DNA supercoiled structures.[37,38]

3 Aggregation dynamics and morphology of the clusters

We begin by analyzing the trajectories of individual fibrils during the aggregation process, tracking their connectivities and chiralities as they evolve with time. To this end, we use *clustering diagrams*, examples of which are presented in Fig. 2. In these diagrams, each fibril is represented by a line, either solid (if it is right-handed) or dashed (for left-handed). The upper panel of Fig. 2 shows the first-order (side-strand) chiralities, whereas the lower panel shows the second-order (backbone) ones.

Let us look more closely at the dynamics of the aggregation process in Fig. 2. Initially, the system contained five fibrils with the helix angle $\alpha_0 = 43.2°$, four of them left-handed and one – right-handed. In the initial stage of the simulation two clusters

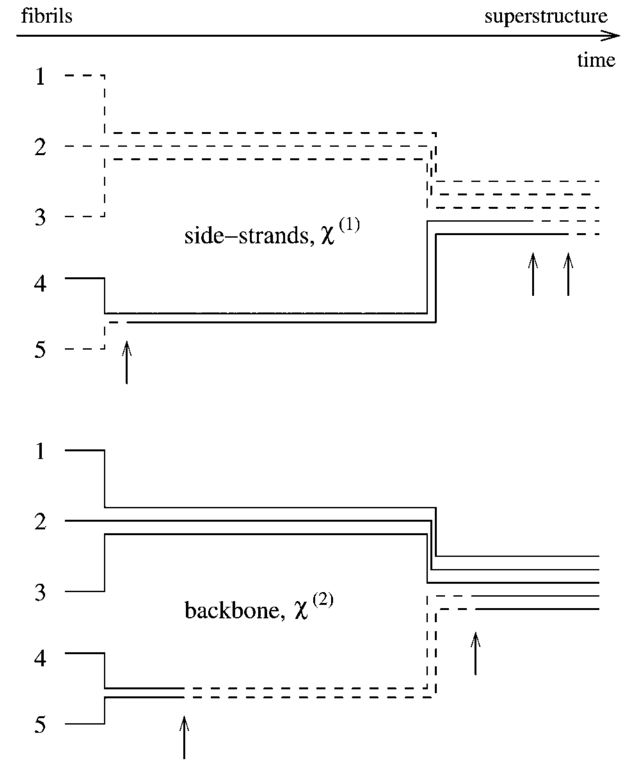

Fig. 2 The clustering diagrams illustrating the dynamics of the aggregation process. Each line corresponds to a single fibril of either right-handed (solid) or left-handed (dashed) chirality. Chiralities of the side strands ($\chi^{(1)}$) are presented in the upper panel whereas the backbone chiralities ($\chi^{(2)}$) are presented in the lower panel. Positions of the lines reflect the connectivities in the clusters and the arrows mark the chirality inversion events.

were created, a two-element and a three-element one. Just after the smaller cluster was formed, one of the fibrils forming it has inverted its first-order chirality to match it to that of its partner. The comparison of the upper and lower panel of Fig. 2 shows that in the larger cluster the chirality of the side strands (L) was opposite to that of the backbone (R). The smaller cluster initially had the same chirality (R) on both levels, soon, however, the backbones have reversed their twists and became left-handed. Subsequently, these two clusters aggregated into a single 5-element cluster with right-handed backbone twist. At that moment, the cluster did not have a uniform side strand twist, with three of its elements left-handed and the other two right-handed. Eventually, however, a common left-handed side strand twist emerged, as a result of chirality inversions of two of its constituents (fibril 4 and fibril 5), which have reversed the sign of both $\chi^{(1)}$ and $\chi^{(2)}$. The final result is a cluster with uniform values of chiralities on both levels – all the fibrils entangle together with the same handedness of backbone twist (R) and maintain the same side strand twist (L).

Let us now analyze the shape of the clusters depending on the twist and handedness of the constituting fibrils. Fig. 3 presents the examples of the aggregates with different values of helix angles of individual fibrils, α_0. Interestingly, there exists a threshold helix angle ($\alpha^* \approx 39° \equiv \lambda_0 = 46°$) above which the first and second-order chiralities of the fibrils in the cluster differ in sign – in other words for $\alpha_0 > \alpha^*$ the fibrils entangle together with handedness opposite to that of individual strands.

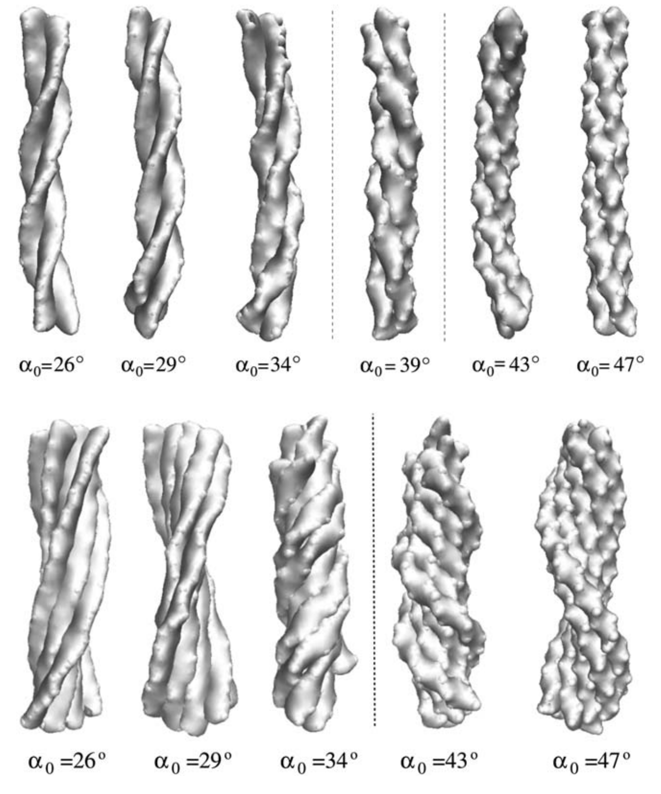

Fig. 3 Example clusters formed of three (top panel) or eight (bottom panel) fibrils. For $\alpha_0 < \alpha^* \approx 39°$ the first- and second order chiralities match, whereas for $\alpha_0 > \alpha^*$ they are of opposite signs. The structure at $\alpha_0 \approx \alpha^*$ is a hybrid one, without a well-defined first-order chirality.

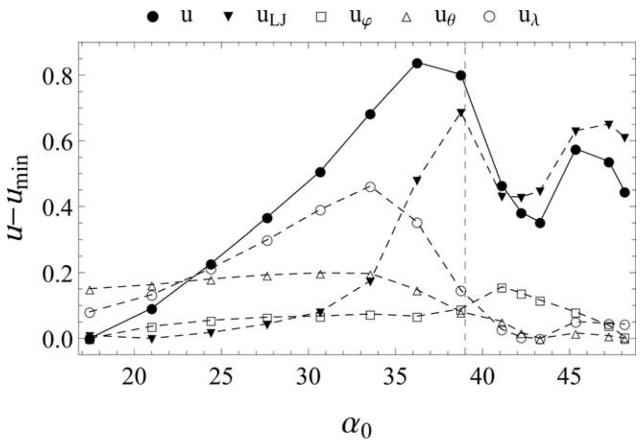

Fig. 4 The contributions to the internal energy per bead, u, of the cluster as a function of the initial helix angle, α_0. The dashed vertical line marks the threshold at which the clusters change the sign of their chirality. For the clarity of presentation, the minimum values were subtracted from each dataset.

The origin of this transition can be understood through exploration of the energy landscape of interconnected fibrils, similar to what was done by Wolgemuth and Sun[39] for the α-helices in the coiled coils. Let us first look at the main contributions to the total energy for the clusters composed of fibrils with different initial α_0. As observed in Fig. 4, for small α_0 the dihedral energy u_λ dominates, while the LJ component is almost at its minimum. This corresponds to the configurations where the fibrils interact in a bead-by-bead manner: each S bead in a side strand meets with its partner on another fibril. This maximizes the number of LJ contacts, but comes at a cost of torsional energy, since the fibrils need to wind around each other, with the twist of the superhelix proportional to the twists of individual subunits. Finally, at $\alpha_0 \approx 35°$ the cost in torsional energy becomes too high and the cluster restructures itself into

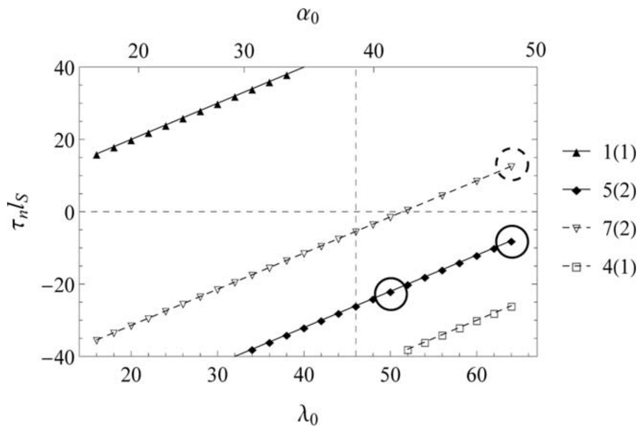

Fig. 5 Effective torsion $\tau_n l_S$ (in degrees) as a function of the initial twist angle (λ_0, lower axis) or the helix angle (α_0, upper axis) for the four basic binding modes, in which every n^{th} side chain bead binds to a neighboring bead on another fibril. The binding modes correspond to $n = 1$ (filled triangles), $n = 5$ (diamonds), $n = 7$ (empty triangles) and $n = 4$ (squares). The modes $n = 5$ and $n = 7$ involve contacts between both side strands of a fibril, as marked in the legend.

a configuration in which every n^{th} side strand bead binds to a neighboring S bead on a second fibril (see Fig. 5). This reduces the twist of the fibril backbone, since the effective torsion is now equal to $\tau_n = \lambda_n/nl_S$, where λ_n is the circumferential angle between a side strand bead and its n^{th} neighbour wrapped to the interval $[-\pi,\pi]$ and $l_S = 2l_{BB}$ is the axial distance between two consecutive S beads of the same side strand. The optimal configuration is then a result of an interplay between the binding energy (which decreases as $1/n$) and torsional deformation, which increases quadratically with τ_n.

Such *binding modes* (characterized by a specific value of n) are reminiscent of the "knobs-into-holes" packing in coiled coils, as described by Crick,[40] where, in the most typical example, α-helices bind by every 7th residue. In the case of α-helices, however, these residues are typically hydrophobic, and the main reason for binding of helices is thus to hide a hydrophobic core. Crick's concepts have been subsequently generalized to the helices of any hydrophobic repeat.[31,41] Interestingly, however, as shown in (ref. 39), out of all the binding modes, the $n = 7$ mode turns out to be optimal in terms of the minimizing of the sum of hydrophobic binding energy and torsional energy of α-helical coiled coils.

Coming back to our structures, the first few binding modes which give the smallest torsion are analyzed in Fig. 5. As already mentioned, for small values of the initial twist, λ_0, the smallest torsions correspond to $n = 1$ mode, *i.e.* the side strands joining in a bead-by-bead manner. This results in the clusters inheriting the handedness from the individual fibrils. In fact, due to the high number of contacts and hence low energy, this mode prevails up to $\lambda_0 \approx 40°$ (or $\alpha_0 \approx 35°$). On the other hand, for $\lambda_0 \geq 46°$ (or $\alpha_0 \geq 39°$) the most energetically favorable is $n = 5$ mode, marked by diamonds in Fig. 5. One should note here that this mode (as well as $n = 7$ mode) involves contacts between both side strands, which doubles the resulting number of binding points (Fig. 6). On the other hand, the modes $n = 1$ and $n = 4$ are characterized by the contacts involving one strand only. This is the reason why $n = 5$ mode becomes more energetically favorable than $n = 4$ mode. The examples of the fibril conformations in this mode for two different λ_0 are given in Fig. 7 and 8. Note that the $n = 5$ mode is characterized by the decreasing torsion with increasing λ_0, hence the structure at $\lambda_0 = 52°$ (Fig. 7) is more twisted than that at $\lambda_0 = 64°$ (Fig. 8). Importantly, this mode corresponds to the negative torsions, hence the handedness of the cluster will be in this case reversed with respect to that of the constituting fibrils.

Finally, for the intermediate values of the twist angles, $35° \leq \alpha_0 \leq 39°$, the two energetically favorable modes $n = 1$ and $n = 5$ compete with each other. As a result, a significant amount of

Fig. 6 The conformation of the fibrils in the $n = 5$ binding mode for $\lambda_0 = 64°$. The figure shows the fibril backbones (grey), side strands (white) and the helical binding seam formed by the contact points (black). Note that the binding seam contains the contacts between both S1 and S2 side strands.

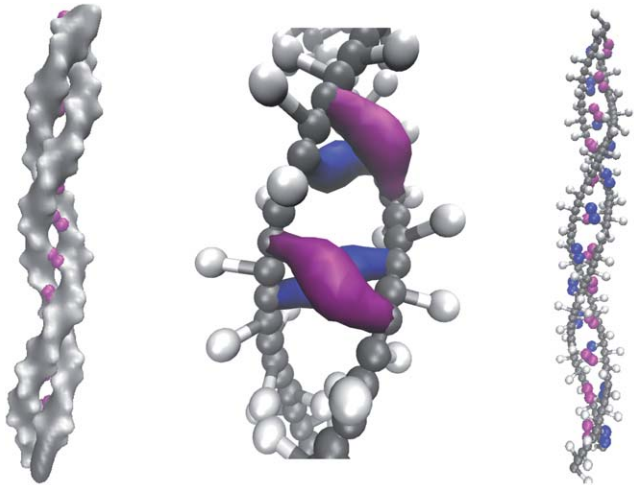

Fig. 7 The detailed conformation of the fibrils in $n = 5$ binding mode for $\lambda_0 = 52°$ ($\alpha_0 = 42°$), corresponding to the left solid circle in Fig. 5. The blue and violet surfaces mark the connections between the beads in contact.

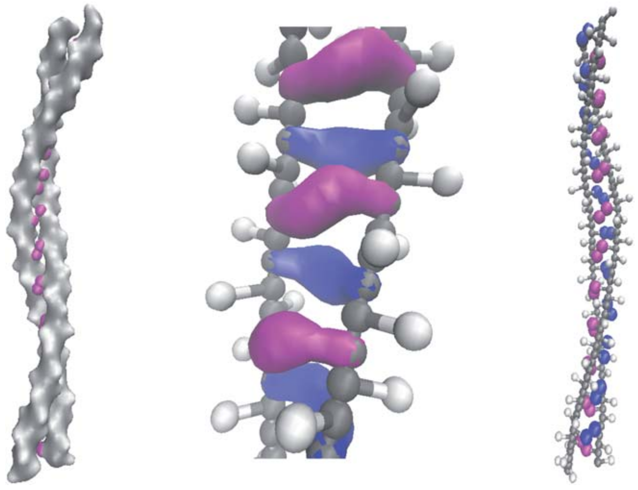

Fig. 8 The conformation of the fibrils in $n = 5$ binding mode for $\lambda_0 = 64°$ ($\alpha_0 = 48°$), corresponding to the right solid circle in Fig. 5. The blue and violet surfaces mark the connections between the beads in contact.

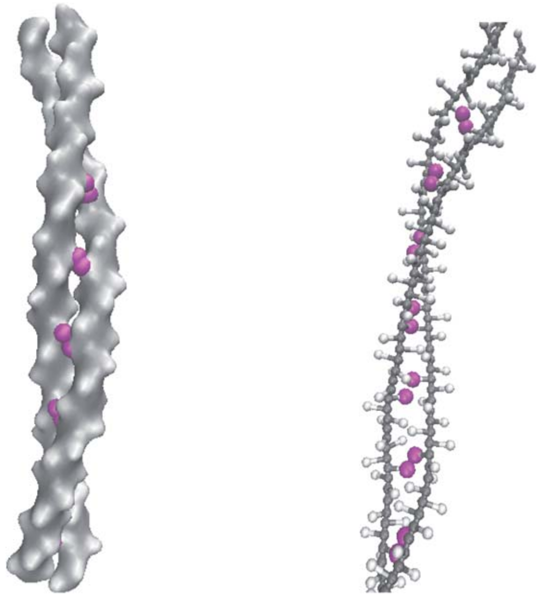

Fig. 9 The conformation of the fibrils in $n = 7$ binding mode for $\lambda_0 = 64°$ (dashed circle in Fig. 5).

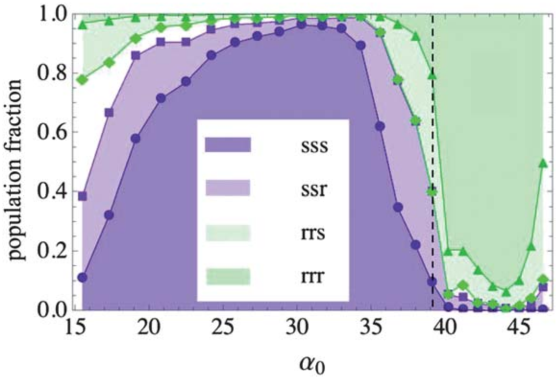

Fig. 11 Synchronization of chiralities within a three-element cluster as a function of the helix angle. The differently colored areas correspond to 'sss' – $\chi^{(1)}$ of all fibrils has the same sign as the respective $\chi^{(2)}$, 'ssr' – one of the fibrils has a reversed chirality, 'srr' – two of the fibrils have the reversed chirality, 'rrr' – all of the fibrils have reversed chiralities (*i.e.* their first-order chirality is different in sign from the second-order one). The vertical axis marks the fraction of the clusters of a given kind.

clusters contain fibrils of different handedness – this is the situation corresponding to the 'hybrid' structure of Fig. 3.

Interestingly, for large α_0 a small number of clusters bind also in $n = 7$ mode, although it is energetically less favorable than $n = 5$ mode due to a small number of side strand contacts. An example conformation of the fibrils connected in that way, corresponding to $\lambda_0 = 64°$, is given in Fig. 9. The effective torsion in this case, $\tau_7 \simeq 13°/l_S$, is positive and thus the cluster is of the same handedness as constituting fibrils.

To analyze the chiralities of self-assembled structures in more detail, we have calculated the average absolute value of the second order chirality of the clusters, $\langle|\chi^{(2)}|\rangle$ as a function of the helix angle of individual strands, α_0 (*cf.* Fig. 10). However, chirality is a signed quantity, hence $\langle|\chi^{(2)}|\rangle$ gives only a limited information about the chiralities in the population. To complement this, we have analyzed the frequencies at which different types of clusters are occurring in the population, comparing the chiralities of the individual fibrils ($\chi^{(1)}$) with the second order chirality ($\chi^{(2)}$) characterising the cluster as a whole. The results (for three-element clusters) are presented in Fig. 11. As expected based on the considerations of Section 3, for $\alpha_0 < \alpha^*$ chiralities of majority of the fibrils are of the same sign as the chiralities of the clusters they belong to, while the reverse holds for $\alpha_0 > \alpha^*$. As already noted, in the interval 35–39° a large fraction of clusters contain fibrils of different handedness. A somewhat similar situation prevails at small α_0, where the relatively low barrier between $\pm\lambda_0$ in the dihedral potential is

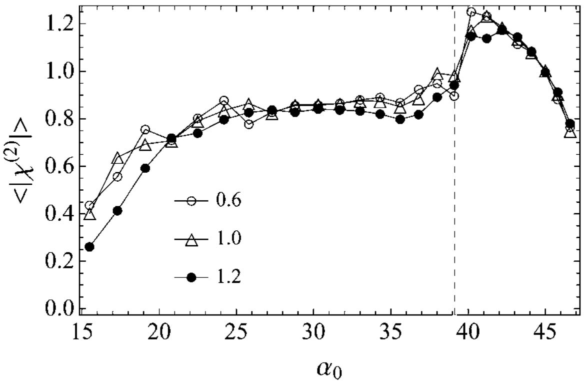

Fig. 10 The average absolute value of the second-order chirality of the cluster as a function of the helix angle, α_0, of individual strands.

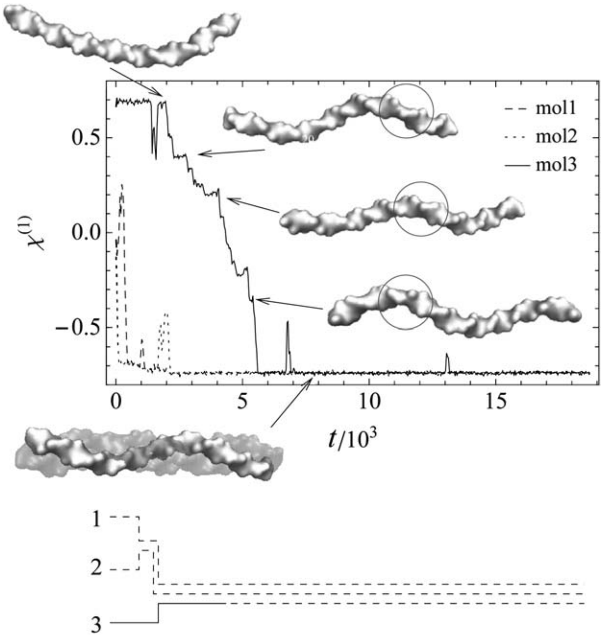

Fig. 12 Chirality inversion process during the formation of a three-element cluster. The first order chiralities of the fibrils are plotted as a function of time, together with a corresponding clustering diagram. Additionally, the snapshots of the morphology of a fibril undergoing the chirality inversion are given (mol 3), with the circle indicating the kink separating left- and right-handed part of the strand. The simulations were carried out at the temperature $T^* = 1.0$ and the initial twist of the fibrils corresponded to $\alpha_0 = 41.2°$.

not strong enough to prevent the thermally induced escape from the potential well.

4 Chirality inversions

As already elucidated in Section 3, a major role in the emergence of the uniform chiral ordering in the aggregates is played by the chirality inversion events, marked by arrows in Fig. 2. A careful analysis of chirality evolution, Fig. 12, reveals that during such an inversion the twist of the molecules changes gradually, over hundreds of timesteps. In fact, the first-order chirality reversal is accompanied by a helical wave propagation, with a kink separating left-handed and right-handed regions moving along the chain, as illustrated in Fig. 12 and 13. Since the kink is the only place along the chain where the values of consecutive dihedrals are uncorrelated, it is associated with a pronounced peak in the dihedral energy (*cf.* Fig. 13). The movement of the kink takes place by a similar mechanism to that driving the movement of defect walls in crystals – the amount of energy required to move the kink one step is of the order of the barrier height in the dihedral potential, much smaller than the energy required to reverse the twist of all the segments at once. In single filaments, the reversal can thus be induced spontaneously due to the thermal fluctuations – the motion of the kink is then diffusive with a characteristic timescale proportional to the square of the length of the fibril. In such a case the chirality reversals are unbiased and the system spends approximately half of the time in left- and right-handed state respectively. In the clusters, the presence of other molecules biases the fibril chirality towards that of its neighbours. This provides the mechanism of chirality synchronization within a cluster. The cluster as a whole can also reverse its chirality, but this happens over much longer timescales than the reversals of individual fibrils.

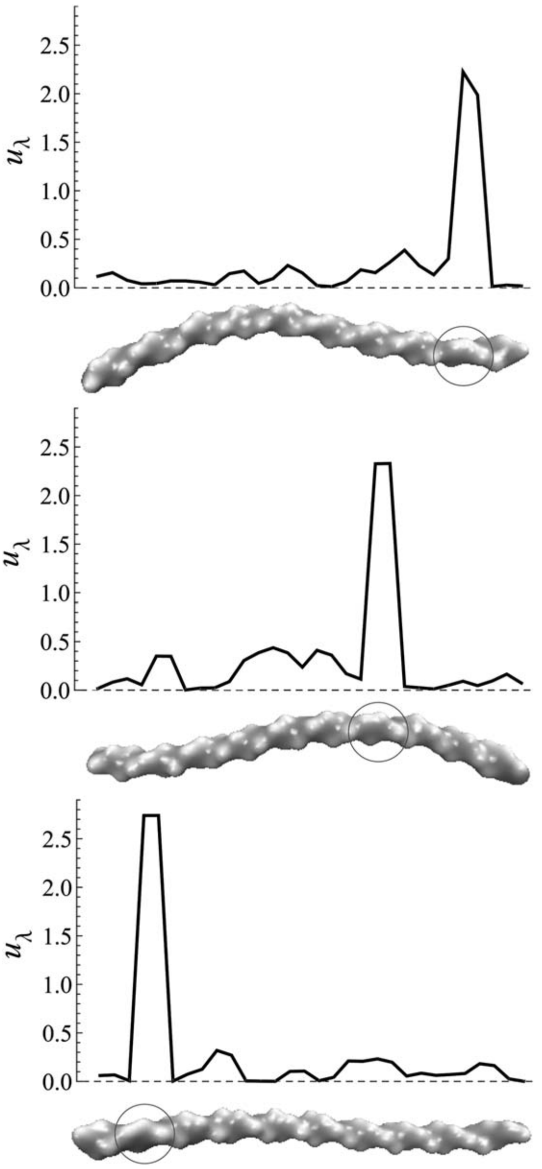

Fig. 13 The distribution of dihedral energy u_λ per bead along the fibril chain during the inversion process. The maximum of the energy is correlated with the position of the kink separating the regions of right- and left-handed twist as it moves along the chain during the inversion process.

Finally, let us analyze frequencies and durations of chirality inversion events. Fig. 14 shows the durations of the chirality inversion, t_r, both for single fibrils as well as for fibrils in the three-element clusters. In the former case, the duration of the inversion event is a monotonically increasing function of the helix angle, the less steep the higher the temperature. A

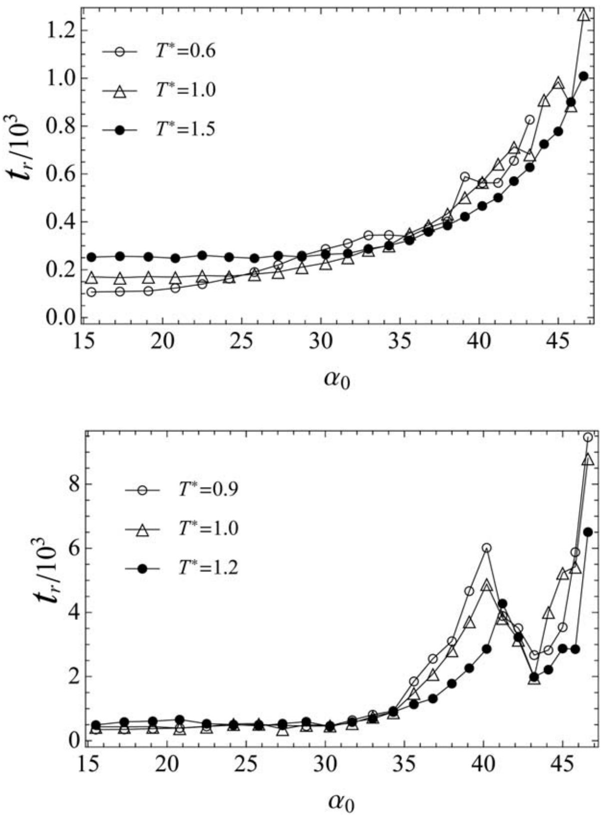

Fig. 14 The duration of the chirality inversion process as a function of the helix angle for a single fibril (upper panel) and for the fibrils in a three-element cluster (lower). The different curves correspond to different temperatures, as marked.

much more interesting case is that of the inversions in the clusters. Here, after an initial increase of t_r with a helix angle, first a strongly peaked maximum appears at $\alpha_0 \approx 40°$, followed by a pronounced minimum at $\alpha_0 \approx 43°$. It is instructive to compare this dependence with the similar dependence for the mean number of chirality inversions per unit time, n_r, shown in Fig. 15. Note that in general, $\frac{1}{n_r} = t_r + t_w$, where t_w is the waiting time for the inversion process to be initiated. At small helix angles (corresponding to low barriers of the dihedral potential U_λ) the inversions can be easily started and $t_w \ll t_r$. However, as the helix angle α_0 increases, it becomes increasingly harder to initiate the inversion process and the ratio of the waiting time to the inversion time rises, most dramatically in the low temperature regime, *e.g.* for $T^* = 0.6$ and $\alpha_0 = 30°$ one gets $t_w/t_r \approx 5$ (again, for a single fibril). In the clusters, the interplay of waiting and inversion times is even more complex. Most notably, there is a pronounced maximum in $n_r(\alpha_0)$ dependence at $\alpha_0 = 35$–$40°$, which at first seems hard to reconcile with the corresponding maximum in $t_r(\alpha_0)$ dependence. In fact, what happens here is that a sharp rise in the inversion times is accompanied by an even sharper decrease of the corresponding waiting times. This can be interpreted by noting that this angle range corresponds to the threshold helix angle α^* at which the first order chirality changes sign with respect to the second order one. In this range, it is particularly easy to initiate the chirality reversal process, but, at the same time, it takes a relatively long time to complete it, because of a large number of backtracking steps involved in the transition between the initial and final chirality. A similar mechanism stands behind the inversion of $n_r(T)$ dependences for a single fibril at small α_0 with respect to those at large α_0: in the former case, somewhat counterintuitively, a higher temperature leads to the decrease of the number of inversions per unit time and simultaneous increase of the inversion times (the waiting times are negligible in this parameter range). Again, for a single fibril at small α_0 it becomes very easy to initiate the inversion process, because of the small height of the barrier, but it gets hard to complete it, because of the large amount of backtracking involved.

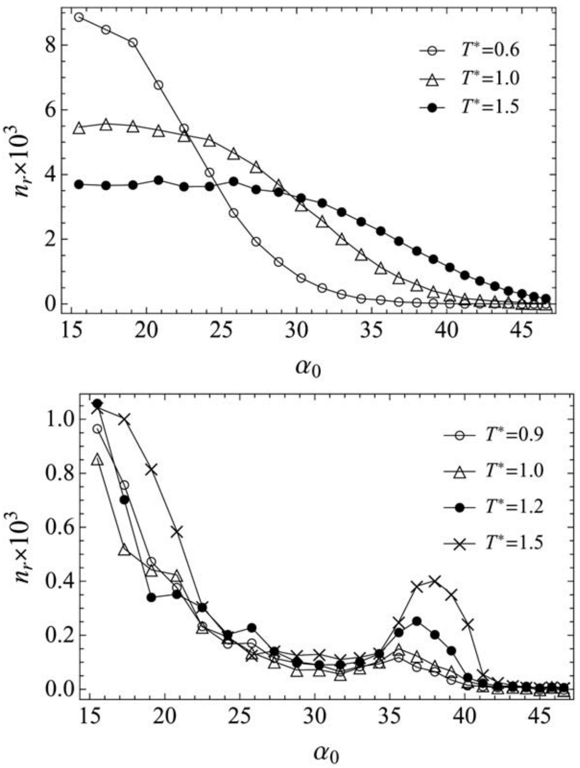

Fig. 15 The average number of chirality inversions per unit time as a function of the helix angle for a single fibril (upper panel) and for the fibrils in a three-element cluster (lower). The different curves correspond to different temperatures, as marked.

5 Summary

In summary, we have presented a simple, coarse-grained model of aggregating chiral fibrils and analyzed the dependence of the morphology of emerging clusters on the initial fibril twist and the temperature. While the latter does not much influence the cluster morphology within the studied parameter range, the former, initial twist of the fibrils, has a significant impact on the handedness of the resulting aggregate. In particular, there exists a threshold initial pitch (corresponding to the helix angle $\alpha^* \approx 39°$) above which the fibrils entangle together with handedness opposite to that of individual strands. This chirality transition has been shown to be associated with the change of the binding mode between the side strands of the fibrils – from the mode in which they bind one-by-one to the mode in which they bind by every 5th side strand bead.

We have also analyzed the evolution of chirality during the aggregation process. As the individual fibrils aggregate, they tend to change their chirality to accommodate it with that of the others. The accommodation process entails a number of chirality inversion events, in which a kink separating right-handed and left-handed regions moves along the chain. In general, the frequency of inversion events decreases with the increasing helix angle, except for the anomaly in the critical region $\alpha_0 \approx \alpha^*$, where it is particularly easy to initiate the inversion process.

Even though these results were obtained with a specific model of the interacting fibrils, some of the conclusions are expected to be relevant for a wider class of systems. In particular, the interplay between the binding energy and the torsional energy will in general induce one or more transitions between different binding modes in the system, some of them accompanied by a global change of chirality. In particular, we hypothesize that a transition of this kind might be the underlying reason for the chiral bifurcation phenomena reported in ref. 13–16.

Acknowledgements

WD and PS acknowledge the support of the Polish Ministry of Science and Higher Education (grant no. N N301 101236). MG acknowledges support of the Foundation for Polish Science (FNP) through TEAM/2010-6/2 project co-financed by the EU European Regional Development Fund, and the PL-Grid

Infrastructure (grant ID: plgly, Hydra Supercomputer). Helpful discussions with Rob Kusner on the intricacies of chiral systems are gratefully acknowledged.

References

1 A. Aggeli, I. A. Nyrkova, M. Bell, R. Harding, L. Carrick, T. C. B. McLeish, A. N. Semenov and N. Boden, *Proc. Natl. Acad. Sci. U. S. A.*, 2001, **98**, 11857–11862.

2 S. Pieraccini, S. Masiero, A. Ferrarini and G. Piero Spada, *Chem. Soc. Rev.*, 2011, **40**, 258–271.

3 N. Rubin, E. Perugia, M. Goldschmidt, M. Fridkin and L. Addadi, *J. Am. Chem. Soc.*, 2008, **130**, 4602–4603.

4 N. Nandi and B. Bagchi, *J. Phys. Chem. A*, 1997, **5639**, 1343–1351.

5 J. V. Selinger, M. S. Spector and J. M. Schnur, *J. Phys. Chem. B*, 2001, **105**, 7157–7169.

6 R. Selinger, J. Selinger, A. Malanoski and J. Schnur, *Phys. Rev. Lett.*, 2004, **93**, 158103.

7 F. Chiti and C. M. Dobson, *Annu. Rev. Biochem.*, 2006, **75**, 333–366.

8 N. Rubin, E. Perugia, S. G. Wolf, E. Klein, M. Fridkin and L. Addadi, *J. Am. Chem. Soc.*, 2010, **132**, 4242–4248.

9 J. L. Jiménez, E. J. Nettleton, M. Bouchard, C. V. Robinson, C. M. Dobson and H. R. Saibil, *Proc. Natl. Acad. Sci. U. S. A.*, 2002, **99**, 9196–9201.

10 J. Adamcik and R. Mezzenga, *Soft Matter*, 2011, **7**, 5437–5443.

11 D. Kurouski, R. K. Dukor, X. Lu, L. A. Nafie and I. K. Lednev, *Chem. Commun.*, 2012, **48**, 2837–2839.

12 D. Kurouski, R. K. Dukor, X. Lu, L. A. Nafie and I. K. Lednev, *Biophys. J.*, 2012, **103**, 522–531.

13 W. Dzwolak, A. Loksztejn, A. Galinska-Rakoczy, R. Adachi, Y. Goto and L. Rupnicki, *J. Am. Chem. Soc.*, 2007, **129**, 7517–7522.

14 A. Loksztejn and W. Dzwolak, *J. Mol. Biol.*, 2008, **379**, 9–16.

15 A. Loksztejn and W. Dzwolak, *J. Mol. Biol.*, 2010, **395**, 643–655.

16 V. Babenko, T. Harada, H. Yagi, Y. Goto, R. Kuroda and W. Dzwolak, *Chirality*, 2011, **23**, 638–646.

17 Z. Y. Yang, M. Zhao, P. X. Lu and Y. F. Lu, *Opt. Lett.*, 2010, **35**, 2588–2590.

18 Z. Yang, P. Zhang, P. Xie, L. Wu, Z. Lu and M. Zhao, *Front. Optoelectron.*, 2012, **5**, 248–255.

19 M. I. Ivanova, S. A. Sievers, M. R. Sawaya, J. S. Wall and D. Eisenberg, *Proc. Natl. Acad. Sci. U. S. A.*, 2009, **106**, 18990–18995.

20 V. Babenko and W. Dzwolak, *FEBS Lett.*, 2013, **587**, 625–630.

21 S. Plimpton, *J. Comput. Phys.*, 1995, **117**, 1–19.

22 M. Osipov, B. Pickup and D. Dunmur, *Mol. Phys.*, 1995, **84**, 1193–1206.

23 A. Ferrarini and P. L. Nordio, *J. Chem. Soc., Perkin Trans. 2*, 1998, 455–460.

24 A. B. Harris, R. D. Kamien and T. C. Lubensky, *Rev. Mod. Phys.*, 1999, **71**, 1745.

25 M. Solymosi, R. J. Low, M. Grayson and M. P. Neal, *J. Chem. Phys.*, 2002, **116**, 9875.

26 G. Raos, *Macromol. Theory Simul.*, 2002, **11**, 739–750.

27 J. I. Kwiecińska and M. Cieplak, *J. Phys.: Condens. Matter*, 2005, **17**, S1565.

28 E. Ruch, *Angew. Chem., Int. Ed. Engl.*, 1977, **16**, 65–72.

29 P. W. Fowler, *Symmetry Cult. Sci.*, 2003, **16**, 321–334.

30 G. Millar, N. Weinberg and K. Mislow, *Mol. Phys.*, 2005, **103**, 2769–2772.

31 A. N. Lupas and M. Gruber, Advances in Protein Chemistry, in *Fibrous Proteins: Coiled-Coils, Collagen and Elastomers*, ed. D. Parry and J. Squire, Elsevier, 2005, vol. 70, pp. 37–78.

32 F. Tombolato and A. Ferrarini, *J. Chem. Phys.*, 2005, **122**, 54908.

33 F. Tombolato, A. Ferrarini and E. Grelet, *Phys. Rev. Lett.*, 2006, **96**, 258302.

34 E. Barry, D. Beller and Z. Dogic, *Soft Matter*, 2009, **5**, 2563–2570.

35 H. H. Wensink and G. Jackson, *J. Phys.: Condens. Matter*, 2011, **23**, 194107.

36 P. Prybytak, W. J. Frith and D. J. Cleaver, *Interface Focus*, 2012, 651–657.

37 A. D. Bates and A. Maxwell, *DNA Topology*, Oxford University Press, 1993.

38 R. Cortini, A. A. Kornyshev, D. J. Lee and S. Leikin, *Biophys. J.*, 2011, **101**, 875–884.

39 C. W. Wolgemuth and S. X. Sun, *Phys. Rev. Lett.*, 2006, **97**, 248101.

40 F. Crick, *Acta Crystallogr.*, 1953, **6**, 689–697.

41 G. Offer, M. R. Hicks and D. N. Woolfson, *J. Struct. Biol.*, 2002, **137**, 41–53.